UCLA
UCLA Previously Published Works

Title

Contrasting Intraurban Signatures of Humid and Dry Heatwaves over Southern California

Permalink

Journal

ISSN

Authors

Shreevastava, Anamika
Raymond, Colin
Hulley, Glynn C

Publication Date

DOI

Copyright Information

Peer reviewed

Contrasting Intraurban Signatures of Humid and Dry Heatwaves over Southern California

ANAMIKA SHREEVASTAVA,[a] COLIN RAYMOND,[a,b] AND GLYNN C. HULLEY[a]

[a] *Jet Propulsion Laboratory, California Institute of Technology, Pasadena, California*
[b] *Joint Institute for Regional Earth System Science and Engineering, University of California, Los Angeles, Los Angeles, California*

ABSTRACT: Heatwaves in California manifest as both dry and humid events. While both forms have become more prevalent, recent studies have identified a shift toward more humid events. Understanding the complex interactions of each heatwave type with the urban heat island is crucial for impacts but remains understudied. Here, we address this gap by contrasting how dry versus humid heatwaves shape the intraurban heat of the greater Los Angeles area. We used a consecutive contrasting set of heatwaves from 2020 as a case study: a prolonged humid heatwave in August and an extremely dry heatwave in September. We used MERRA-2 reanalysis data to compare mesoscale dynamics, followed by high-resolution Weather Research and Forecasting modeling over urbanized Southern California. We employ moist thermodynamic variables to quantify heat stress and perform spatial clustering analysis to characterize the spatiotemporal intraurban variability. We find that, despite temperatures being $10° \pm 3°$C hotter in the September heatwave, the wet-bulb temperature, closely related to the risk of human heat stroke, was higher in August. While dry and humid heat display different spatial patterns, three distinct spatial clusters emerge based on nonheatwave local climates. Both types of heatwaves diminish the intraurban heat stress variability. Valley areas such as San Bernardino and Riverside experience the worst impacts, with up to $6° \pm 0.5°$C of additional heat stress during heatwave nights. Our results highlight the need to account for the disparity in small-scale heatwave patterns across urban neighborhoods in designing policies for equitable climate action.

SIGNIFICANCE STATEMENT: Heatwaves are the leading cause of morbidity and mortality among all environmental hazards. Moreover, their frequency and intensity are on the rise due to climate change. Southern California is no stranger to extreme heat, but persistently humid heatwaves still test the adaptability limits of its residents. We find that the set of two contrasting heatwaves that afflicted Los Angeles in the summer of 2020 forms the perfect testbed for characterizing the impacts of humid versus dry heatwaves on urban environment. Because climate model forecasts and long-term observational trends point to more humid heatwaves in the future for Southern California, our results underscore the importance of including moist heat in extreme heat warning frameworks.

---

1. Introduction

Extreme heat events are one of the deadliest and most rapidly increasing weather hazards, and they also exert substantial effects on cognition and labor productivity (Vicedo-Cabrera et al. 2021; Borg et al. 2021; Goodman et al. 2019; Dunne et al. 2013; Cedeño Laurent et al. 2018; Parsons et al. 2022). Heatwaves (HW) are generally the result of heating from subsidence and radiation due to anticyclonic circulation patterns in a region of more than 1000 km², exacerbated by stagnant air in the boundary layer that prevents the dissipation of trapped heat (Black et al. 2004; Zhao et al. 2018). Although there is no standard temperature threshold that characterizes HWs, they are often identified as locally anomalous high temperatures or heat stress (based on historic percentiles) that persist for three or more consecutive days (Robinson 2001). During the last decade, HWs have increased in intensity, frequency, and duration in many places due to climate change, and the trend continues to increase (Meehl and Tebaldi 2004; Perkins-Kirkpatrick and Lewis 2020; Schwingshackl et al. 2021; Brown 2020). This equates to an increase in empirically associated heat conditions with mortality and adverse health outcomes such as exhaustion, cardiovascular events, or pregnancy complications (Mora et al. 2017; Vanos and Grundstein 2020). Intense humid heat, in particular, is causing the heat-stress adaptability limit for humans to be approached ever more closely (Raymond et al. 2020; Speizer et al. 2022; Sherwood and Huber 2010). Yet, extreme heat tends to receive less attention than counterparts such as severe storms (Orth et al. 2022).

Because of its geography and subtropical location, Southern California has regularly experienced intense extreme heat during the observed record and has seen an increase in HW metrics such as duration, frequency, and severity over the past few decades, particularly in densely populated urban

---

regions (Gershunov et al. 2021; Hulley et al. 2020; Tamrazian et al. 2008). The region is typified by a semiarid Mediterranean climate with warm, dry summer days and comfortable nights. In the twentieth century, most of its HWs were dry, with the most notable feature being high daytime maximum temperatures (Gershunov et al. 2009). However, Southern California is witnessing a shift toward more humid heatwaves with higher minimum temperatures at night under observed warming (Hulley et al. 2020; Gershunov et al. 2009; Gershunov and Guirguis 2012). This increase in humidity has been hypothesized to be connected, at least in part, with increasing upwind sea surface temperatures (Pierce et al. 2006; Gershunov et al. 2009). The exposed population has also grown dramatically, approximately quadrupling since 1950. Therefore, Southern California is a valuable testbed for studying the mechanisms that lead to dry versus humid HW.

Here, we examine a case study of two HWs that affected the Southern California region in the summer of 2020. The first event, referred to hereafter as the August HW, extended from 15 to 28 August 2020. It was characterized by hot and humid conditions that persisted for nearly two weeks. It was followed by a short but more intense 3-day period (5–7 September) accompanied by extremely dry conditions. We first characterize both HWs using the Modern-Era Retrospective Analysis for Research and Applications, version 2 (MERRA-2), reanalysis dataset and contrast the summer 2020 case study relative to the historical extreme heat climatology of the region (section 2). We then use the Weather Research and Forecasting Model to simulate the HW and take a closer look at its impact on the urban area of metropolitan Los Angeles (section 3).

The first goal of this study is to compare and contrast the dry and humid HWs in our summer 2020 case study over Los Angeles. Previous literature has shown that HW impacts differ according to their relative humidity: humid events lead to increased concerns about health, productivity, and energy demand (Laaidi et al. 2012; Vant-Hull et al. 2018; Stone et al. 2021; Dunne et al. 2013), while dry events can stress terrestrial and aquatic ecosystems, lead to crop failures, and increase the probability of wildfires (Raymond et al. 2019; Lesk et al. 2021; Gutierrez et al. 2021). In this paper, we characterize a HW's "impact" as the *additional heat stress* that it caused for urban inhabitants of the region, compared to the non-HW days of 2020. This is quantified using a suite of heat stress indices (Buzan et al. 2015) that consider air temperature, specific humidity, and solar radiation (section 4a).

Our second goal is to study the intraurban variability of heatwave impacts. The Los Angeles metropolitan region is one of the largest urban agglomerations (area = 12 560 km^2 according to the U.S. Census Bureau, comprising a population of ~18 million) with diverse urban morphologies, including expansive suburbs with varying vegetation densities, large industrial zones, and several commercial centers with high-rise buildings. Additionally, there are wide climatological variations in urbanized parts of Los Angeles, ranging from coastal neighborhoods that rarely exceed 25°C to inland valleys with summer daytime temperatures around 38°C. Not only does this yield a heterogeneous urban heat island (UHI) as in other cities (Shreevastava et al. 2019a; Sobstyl et al. 2018; Zhou et al. 2017),

but this UHI can interact differently with the same synoptic HW forcing, yielding spatially and temporally variable intraurban heat islets (Shreevastava et al. 2019b, 2021). We explore the patterns in spatial variability of heat stress within urban neighborhoods by applying a spatial clustering algorithm (section 4b). Through the lens of this case study, our objective is to understand more broadly how HW temperature and humidity anomalies vary across a heterogeneous landscape, and how these patterns may differ under different regional circulation regimes.

2. Characterizing the Southern California HWs of 2020

Southern California is situated at the interface between two regimes that influence the humidity of high-heat days in opposite ways. In Fig. 1, we show the relative humidity climatology for the top 1% of highest heat stress (computed as wet-bulb temperature) days of California in comparison with the rest of the continental United States, evaluated for the 1980–2020 period. In the Pacific Northwest and the Central Valley of California, the most intense heat stress is experienced as a result of drier, hot conditions, whereas in the interior of the Southwest it is driven by higher humidity (Fig. 1a). This results in a larger range of relative humidities on hot days in California than anywhere else in the United States (Fig. 1b). These patterns are associated with large-scale high pressure systems (causing downslope winds, warm-air advection, and/ or high solar radiation due to absence of cloud), and with moisture from the North American monsoon (Raymond et al. 2017). In the eastern United States (east of 100°W), temperature and moisture are more closely related, and relative humidity anomalies during the HWs are small (Fig. 1a).

California HWs can be dominated by either of the two general mechanisms noted above, and this is the case for both the Central Valley and coastal areas, although in different proportions (Gershunov et al. 2009; Lee and Grotjahn 2016). This results in two types of heatwaves: typically daytime accentuated (characteristically dry), and nighttime accentuated (characteristically humid) HWs (Gershunov and Guirguis 2012). Although dry HWs have seen interdecadal variations, nighttime accentuated humid events have steadily increased in intensity since 1950 (Hulley et al. 2020). The trends are attributable to urbanization, general atmospheric warming, and an anomalous moisture source off the coast of Baja California associated with sea surface warming (Pierce et al. 2006; Hulley et al. 2020). Further changes are projected to be strongest along the coasts, where the majority of the population is located (Gershunov and Guirguis 2012).

The contrasting HW mechanisms were neatly illustrated within a span of a few weeks in summer 2020. In mid-August, an anticyclone developed over the western United States and remained nearly stationary for about two weeks. A southwest–northeast-tilted ridge and a strong surface low off the California coast led to a southeasterly onshore flow over greater Los Angeles, simultaneously precluding the typical northwesterly flow and cold upwelling currents that bring cooler air into the region (Fig. S1 in the online supplemental material). This caused positive anomalies of both temperature and moisture, particularly because of the unusually large meridional
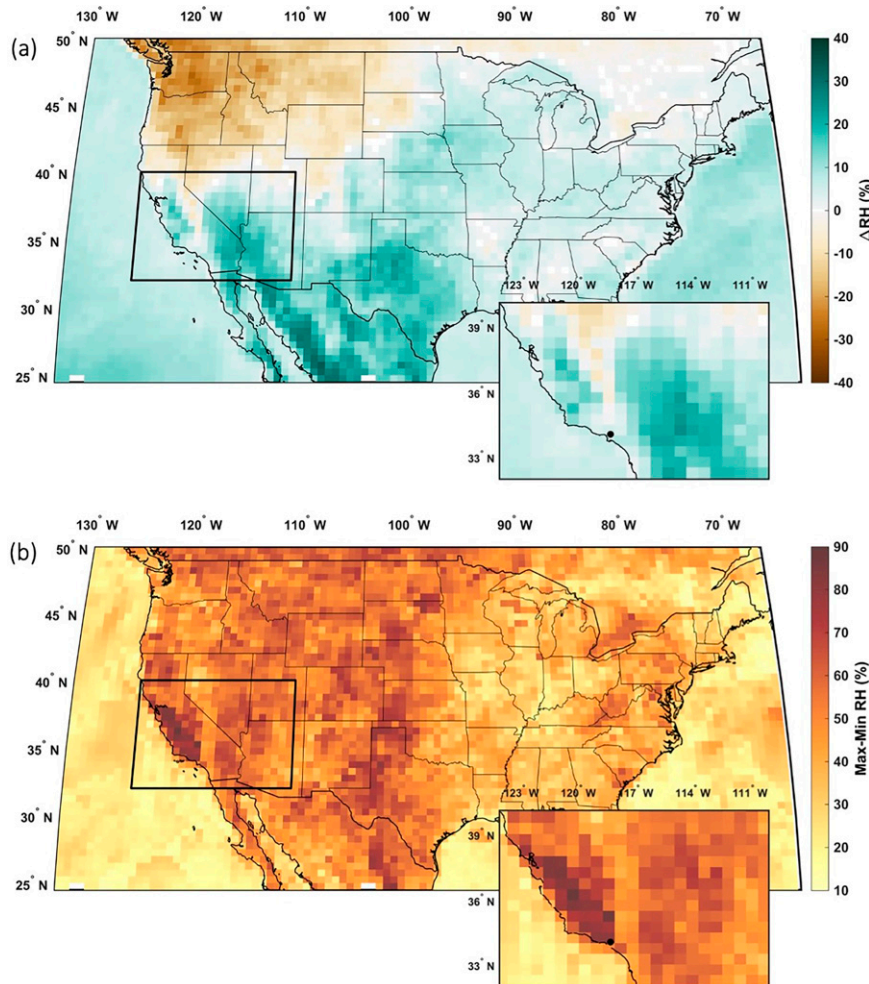
FIG. 1. (a) RH of the top-1% heat-stress days, as an anomaly from the annual-mean RH. Regions in brown experience their most intense heat stress as a result of hot and dry conditions, whereas for those in green it is driven by anomalous humidity. (b) Range of RH (difference between maxima and minima) for the same region. Data are from MERRA-2. The inset shows Southern California where maximum variability in humidity for extreme heat days occurs.

gradient of sea surface temperature along the Baja California coast. The August HW exhibits characteristics of downslope warming from the mountains north and east of Los Angeles combined with an anomalous coastal influence due to the southerly wind component. This is typical of seasonal monsoon winds in the region as shown in Fig. S1. Furthermore, it closely matches previous depictions of humid heat-related winds in this region (see Hulley et al. 2020, Fig. 5b).

Several weeks later, a shorter but more intense anticyclone centered over Oregon with 500-hPa geopotential height anomalies of 150 m drove north or easterly (offshore) flow in Southern California (Fig. S1). Importantly, these low-level wind conditions, channeled and enhanced by topography and thermal gradients, can be highly localized and not well captured by larger-scale representations. The stronger winds, especially near the surface, led to extreme heat and aridity via adiabatic warming and a minimization of typical oceanic cooling (from 5 to 7 September). Afternoon temperatures broke the Los Angeles County daily maximum air temperature record, reaching 49.5°C in the San Fernando Valley (https://earthobservatory.nasa.gov/images/147256/california-heatwave-fits-a-trend). These conditions also sparked and fanned the flames of the Bobcat fire in the San Gabriel Mountains that border the urbanized area, with the ultimate destruction of 170 structures (Safford et al. 2022). We find that both of these HWs brought temperatures above the 90th percentile of the August–September climatology, computed using a 7-day moving window based on 40 years of MERRA-2 data, from 1980 to 2019 (Fig. S2 in the online supplemental material).

3. Data and methods

a. WRF Model

Our primary dataset for this study is the model output from the Weather Research and Forecasting (WRF) modeling
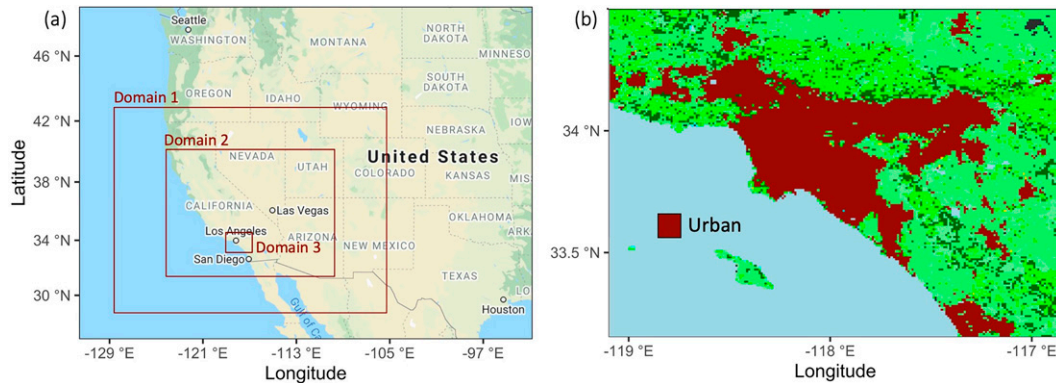
FIG. 2. (a) The nested domain set up used to run the WRF simulation of the 2020 Southern California heatwave. The domain grid resolutions are 9, 3, and 1 km (from domains 1 to 3 respectively). (b) Domain 3 is centered over the metropolitan urban area of Los Angeles. MODIS's LULC is used for spatial characterization. Urban LULC is shown in dark red.

framework. WRF is a fully compressible and nonhydrostatic mesoscale numerical weather prediction model that includes an urban canopy model that allows for a sophisticated representation of land–atmosphere feedbacks in urban areas (Vahmani and Ban-Weiss 2016; Chen et al. 2011). A brief description of the boundary conditions, spatial domain, and selected physics parameterizations is presented below, and for research reproducibility the namelist files are included as Text S1 in the online supplemental material.

Simulations are carried out on three nested grids, centered in the Los Angeles metropolitan area, with horizontal grid resolutions of 9, 3, and 1 km, respectively (Fig. 2a). The land cover–land use (LULC) is characterized using MODIS (product MCD12Q1; Fig. 2b). The model was run for a 45-day period from 1 August 2020 to 15 September 2020, including the two HWs (17 days of heatwave in total), and the remaining non-HW days serve as control (Fig. 4a). The first two simulated days are discarded as model spinup time.

As forcing of the atmospheric boundary condition, NCEP Final Analysis (FNL) operational global analysis and forecast data (spatial resolution 0.25°, temporal resolution 6 h) were used to drive the model. The physical parameterization schemes used in the current study include the Monin–Obukhov scheme for the model surface layer, the Yonsei University (YSU) scheme for the planetary boundary layer (PBL), the Kain–Fritsch cumulus scheme, the Lin scheme for microphysics, the Rapid Radiative Transfer Model for longwave radiation, and the Dudhia scheme for shortwave radiation. For the urban parameterization, the atmosphere model is coupled to the Noah LSM including the single-layer urban canopy model (UCM).

b. Model validation and limitations

The model output for domain 3 is validated against observed data by comparing near-surface (at 2-m height) air temperature (NSAT) as well as land surface temperature (LST). The NSAT is validated first using the National Centers for Environmental Information (NCEI) ground observation network for 21 sites (https://www.ncei.noaa.gov/). Note that the NCEI air observation towers are all located at regional airports. Therefore, although it captures the diurnal thermal

variability of the regions very well, it cannot be treated as a true representative of a mixed-use urban area WRF grid cell.

Most of the locations (14 of 21) have a bias (calculated as $NSAT_{NCEI} - NSAT_{WRF}$) under 2°C, and the stations in southern Los Angeles (LA) have the lowest average bias with values less than 1°C as well as low RMSE values indicating very good agreement of observations with the WRF simulations (Fig. 3). The stations in the inland valleys, such as Riverside, Ontario, and San Bernardino on the eastern side as well as Van Nuys and San Fernando on the western side, have a positive bias ($\sim$2°C) as well as relatively high RMSE values ($\sim$4.5°C). This indicates that the nighttime temperatures in those regions were underestimated by WRF. On the other hand, a negative bias is observed in the case of some coastal stations such as Santa Monica and Los Angeles Airport (LAX), wherein the observed daytime maximum air temperatures are cooler than that simulated by WRF. This is an influence of sea breezes and sharp temperature gradients that may not be very well captured by WRF at a 1-km spatial resolution. As a result, the RMSE values for Santa Monica are also the highest (5.3°C, Fig. 3). The complete time series and air temperature distributions for each NCEI station are given in Table S4 and Fig. S4 in the online supplemental material.

Figure S2 in the online supplemental material further illustrates the WRF differences in wind direction and strength from ERA5-Land but shows that it successfully differentiates the stronger general northerly winds of the September HW from the predominant south/easterly flow of the August HW. The surface temperature WRF output is validated using the standard LST product from the Ecosystem Spaceborne Thermal Radiometer Experiment on the Space Station (ECOSTRESS; Fig. S3 in the online supplemental material). A similar pattern of underestimation of the valley temperatures and an overestimation of the coastal Santa Monica/Malibu area can be seen here as well. Fully investigating the origins of these model biases and accounting for them in future analyses will be important for applying our methods and conclusions to other heatwaves in the study domain and in other regions globally with similar meteorological and geographical characteristics.
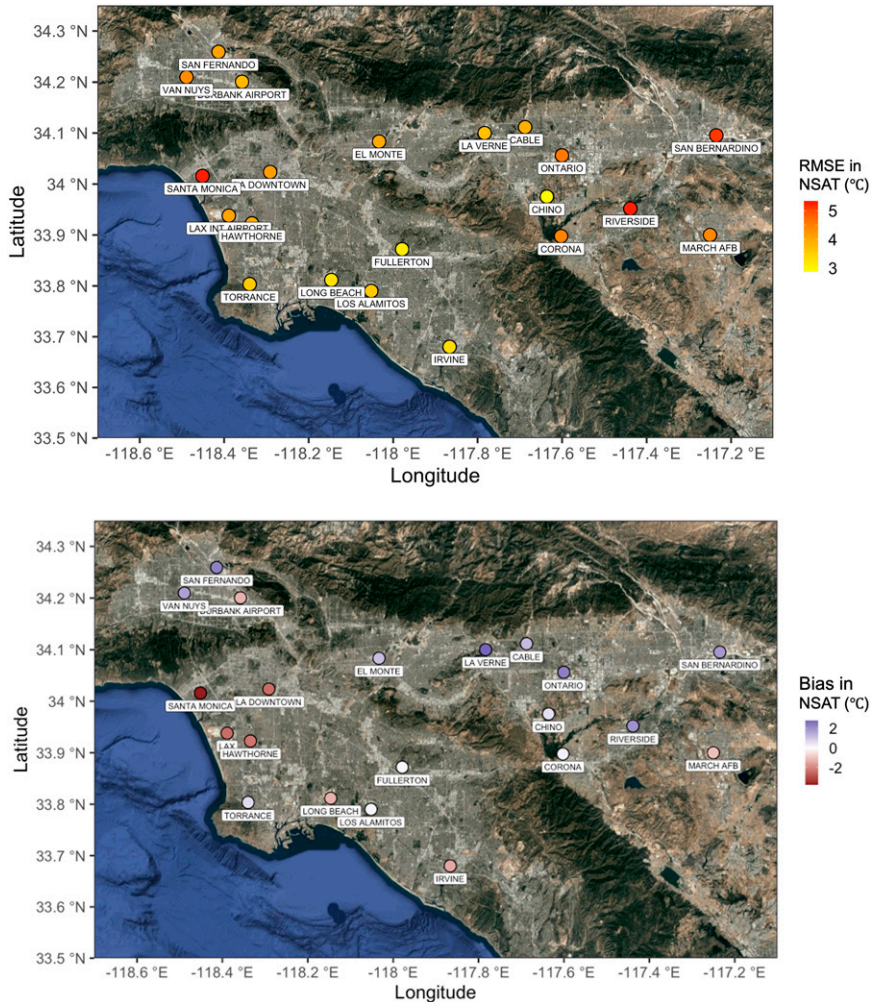
FIG. 3. The NSAT from WRF is validated against the NCEI in situ observation network. Each symbol represents the location of the validation station. The symbol color indicates the (top) average RMSE and (bottom) average NSAT bias values. The bias is calculated as $NSAT_{NCEI} - NSAT_{WRF}$. Positive bias indicates underestimation of temperatures by WRF.

c. Heat stress metrics

We first explore the spatially averaged diurnal time series of excess heat stress for each of the HWs (section 4a). Note that because there is no single standard metric to assess heat stress, we evaluated heat stress in three layers of increasing complexity by employing different thermal comfort indices. First, we consider only the NSAT (estimated at about 2 m above the ground) as a measure of sensible heat. This is a standard model output variable from WRF. Next, we use the wet-bulb temperature (WBT), which is a moist thermodynamic quantity that correlates with heat stress for humans by accounting for the impact of humidity, relative humidity (RH) in this case, which alters the ability to cope with extreme heat by sweating (Sherwood and Huber 2010; Buzan and Huber 2020). We compute this using NCAR Command Language (https://www.ncl.ucar.edu/Document/Functions/Built-in/wrf_wetbulb.shtml) diagnostic package (Stipanuk 1973). The

thermal gradients in NSAT and WBT, as well as excess heat stress (characterized as ΔNSAT and ΔWBT and calculated as the difference between HW and corresponding non-HW days), are shown for urban LA in Fig. 6, which is discussed in more detail below. Last, we incorporate the influence of direct solar radiation (SR) by investigating the environmental stress index (ESI).[1] ESI was developed as an alternative to the wet-bulb globe temperature (WBGT) and was thoroughly validated to show that it is highly correlated with WBGT (Moran et al. 2001).

d. Spatial clustering

We also inquire how the HWs impact the different neighborhoods within the urban Los Angeles region (section 4b). To characterize the spatial patterns of the HW impacts, we

---

[1] $ESI = 0.63 \times NSAT - 0.03 \times RH + 0.002 \times SR + 0.0054 \times (NSAT \times RH) - [0.073/(0.1 + SR)]$.
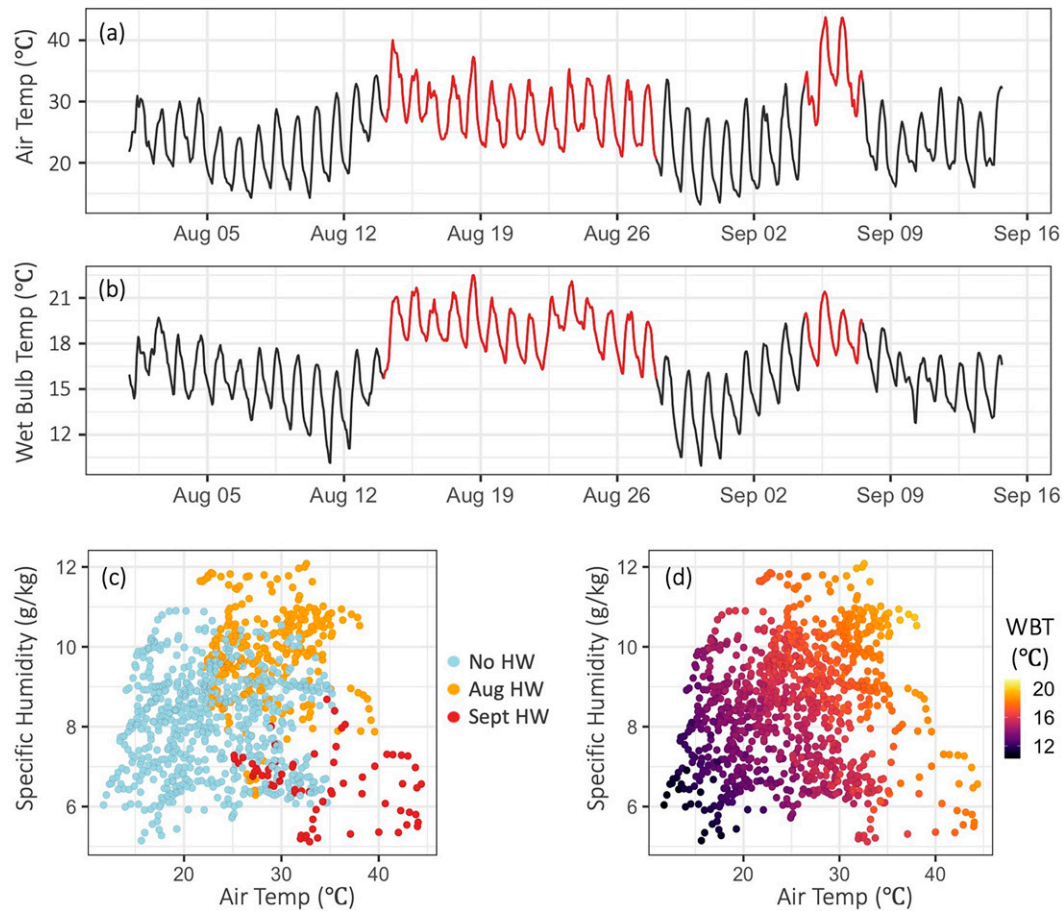
FIG. 4. (a) The time series of spatially averaged NSAT over urban areas for the 45-day period simulated in WRF. The two HWs are highlighted in red. (b) Time series of spatially averaged WBT, shown in a format similar to that of the two HWs shown in red. (c) Scatterplot between air temperature (°C) and specific humidity (g kg^{-1}) for each hour of the simulation. The instances corresponding to the August and September HW are colored orange and red, respectively. The non-HW times are shown in blue. (d) Scatterplot between air temperature (°C) and specific humidity (g kg^{-1}), with the color corresponding to WBT for each time step (every hour of the 45-day simulation). A similar figure with RH on the x axis is included as Fig. S6 in the online supplemental material.

first identified sets of LA neighborhoods that have similar local geography and urban morphology (map provided in Fig. S5 in the online supplemental material). Then we applied a hierarchical clustering algorithm on the diurnal time series of ΔNSAT and ΔWBT. We applied agglomerative clustering, which is a bottom-up approach, where the different LA neighborhoods were grouped together based on the diurnal pattern of response to the HWs. We use the built-in stats function *heatmap* (https://www.rdocumentation.org/packages/stats/versions/3.6.2/topics/heatmap) in the R software package to implement clustering.

4. Results and discussion

a. August versus September HW from heat stress perspective

1) NSAT

To evaluate the time-dependent impact of HWs on air temperatures, we first perform a spatial average of NSAT over all

urban areas (Fig. 2b) to obtain a single time series. We then compute the average temperature for each hour of the day, grouped by August HW, September HW, and non-HW days (Fig. 4a). This is illustrated in Fig. 5a, where the solid lines (in red) correspond to the spatiotemporal mean diurnal trend of air temperature for each of the HWs, and the dashed line shows the diurnal trend for non-HW scenario. Here, the shaded regions represent one standard deviation of spatiotemporal variability for each HW. We then take the difference between the HW and the non-HW scenario to compute the amplification in air temperature caused by each HW. We refer to this variable as ΔNSAT (Fig. 5d). Spatial heterogeneity within NSAT and ΔNSAT is shown in Fig. 6 (top four plots) for the September HW and is discussed in detail in section 4b.

Here, we can see that, according to WRF, both HWs had the strongest impact during the night, and these anomalies are significantly higher for the September HW (ΔNSAT ~ 15°C),
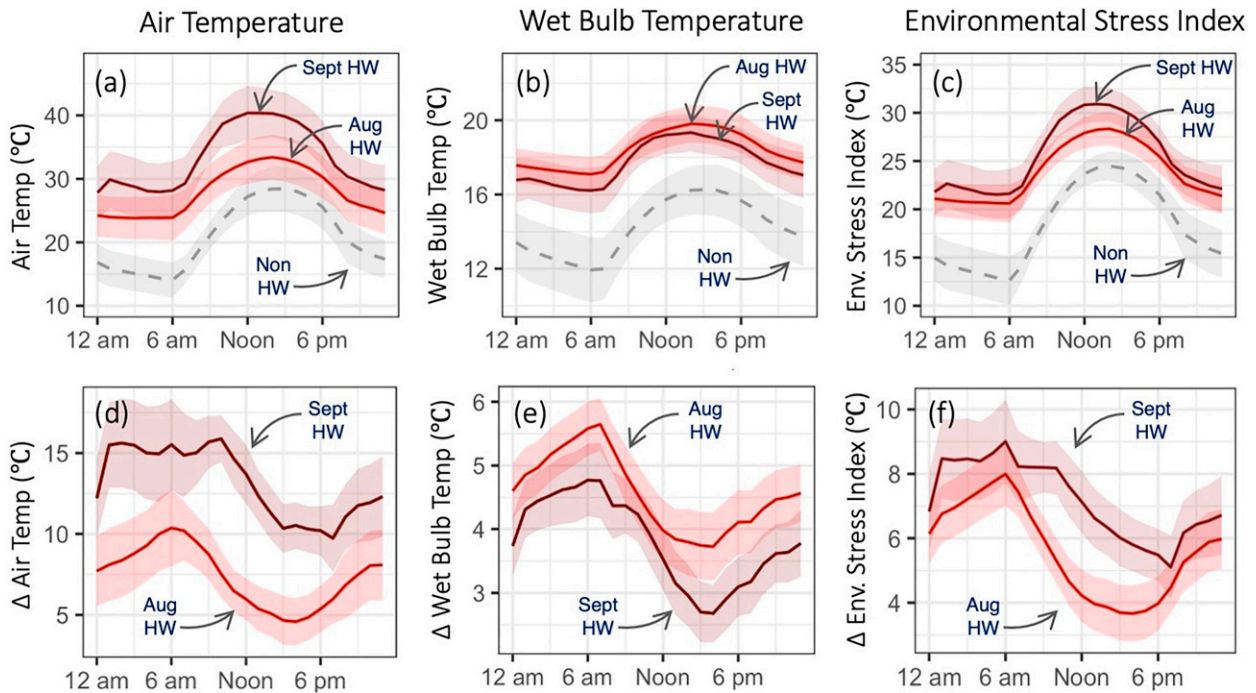
FIG. 5. The average diurnal trends of (a) NSAT, (b) WBT, and (c) ESI (°C) for the conditions of August HW (in red), September HW (in brown), and non-HW (gray with dashed line). Also shown is the average diurnal trend of excess heat characterized by (d) ΔNSAT, (e) ΔWBT, and (f) ΔESI (calculated as the difference between the diurnal trend for HW days and non-HW days) for the August HW in red and the September HW in brown. The solid line indicates the mean (computed as spatial mean over urban areas and then hour-specific averaged over the identified HW or non-HW days), and the colored ribbon corresponds to ±1 standard deviation for each of the variables.

highest in the San Fernando Valley (Fig. 5d and top four plots of Fig. 6). In these WRF simulations, ΔNSAT decreased steadily after sunrise, but the temperatures were still more than 10°C higher than usual throughout the day, resulting in a maximum NSAT ∼ 40° ± 5°C during the afternoon hours (Fig. 6, top four plots). The August HW showed a similar diurnal pattern with the highest amplification of ΔNSAT ∼ 10° ± 2°C around dawn and the lowest ΔNSAT ∼ 5° ± 2°C during the late afternoon hours. As discussed in the methods section, this WRF output exhibits a strong positive nighttime bias for temperature, inverting the true diurnal cycle of anomalies, which is flat or peaks in the afternoon. The WBT anomalies are consistent with reanalysis and observation data during the daytime; the nighttime WRF's temperature anomalies are overestimated by roughly a factor of about 2 (Figs. S8 and S9 in the online supplemental material).

2) WET-BULB TEMPERATURE

The relationship between WBT and NSAT is shown as a scatterplot between specific humidity and NSAT (Figs. 4c,d). The August HW (shown in orange) had the highest humidity during the season accompanied by NSAT in the range of 25°–40°C, and the September HW (shown in red) represents a warmer NSAT (nearly 30°C during the night) but a lower humidity case. These offsetting qualities result in similar WBT (Fig. 4d). Note that, for the same WBT values, higher

temperatures can produce greater discomfort and perceived heat exhaustion in people (Vecellio et al. 2022), especially if we account for the impact of direct solar radiation (quantified as ESI and discussed in detail in the following subsection).

We then perform the same spatiotemporal averaging for WBT over urban areas as previously described to obtain the diurnal trend of WBT (Fig. 5b). We then calculate the excess heat stress (denoted as $\Delta WBT = WBT_{HW} - WBT_{nonHW}$), which indicates how much the heat stress was amplified by HW compared to the remainder of the summer of 2020 (Fig. 5e). Here, as well, WRF suggests that the impact of both HWs was most prominent during the night and especially during the early morning hours. While this is accurately captured in case of the August HW, the September HW nighttime bias in NSAT results in overestimation of ΔWBT during September HW night as well. WRF and observations agree that among the two HWs, the August HW had a higher heat stress than the September HW with a maximum difference during the early morning hours (Figs. S8 and S9 in the online supplemental material). Coupled with the fact that the August HW persisted for 10 days, it produced prolonged exposure to high heat stress, despite a lower NSAT—a major concern for human health (Baldwin et al. 2019). The spatial heterogeneity in WBT and ΔWBT is shown in Fig. 6 for August HW and will be discussed in detail in section 4b.
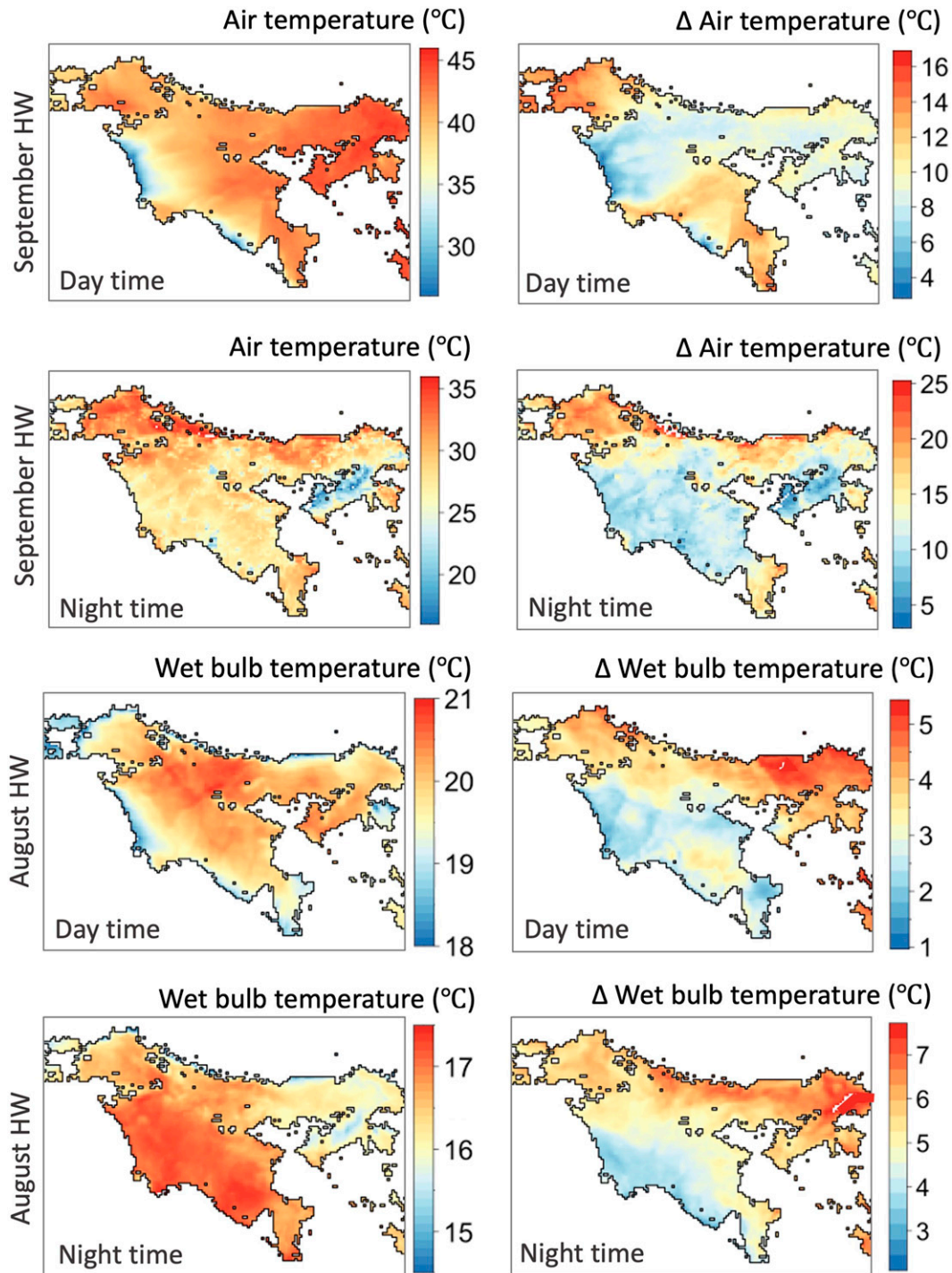
Fig. 6. (left) HW composite thermal maps made by averaging the temperatures for HW nights (from 0200 to 0500 LT) and HW days (from 1200 to 1500 LT), as labeled, for the HW days shown in red in Fig. 4. (right) Excess temperature maps (ΔNSAT and ΔWBT) computed as a difference between the composite HW and non-HW temperatures for both daytime and nighttime, as labeled The top four plots show the average daytime and nighttime NSAT for the September HW as well as the ΔNSAT when compared with the non-HW scenarios. The bottom four plots show the WBT maps during the day and at night for August HW as well as the excess heat stress (ΔWBT) for the same.
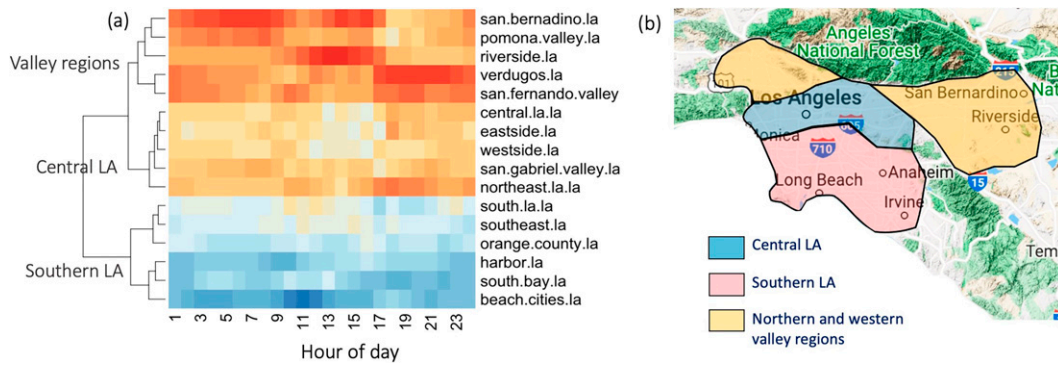
FIG. 7. (a) Dendrogram heat map plot showing the emerging hierarchical clusters of different neighborhoods. The colors represent a unitless scaled ΔWBT relative to the other locations and range from 0 to 1. The time of day is shown along the x axis, and the name of the LA neighborhood is shown on the y axis. The location of these neighborhoods on the LA map is shown in Fig. S5 in the online supplemental material. (b) Map of the three main spatial clusters within the greater Los Angeles urbanized area.

3) ESI

The ESI and WBT are strongly positively correlated and the spread around the correlation is explained by the degree of influence of humidity and solar radiation in each metric. For a given WBT, the ESI increases in proportion to solar radiation, because WBT does not account for solar radiation, whereas, relative to ESI, WBT is more sensitive to the influence of humidity (Fig. S7 in the online supplemental material). We perform spatiotemporal averaging to obtain a diurnal time series for ESI (Fig. 5c) and compute a HW anomaly of it (ΔESI; Fig. 5f). The diurnal trend of ΔESI mimics that of ΔWBT for both the HW with a stronger amplification during the nighttime, but September HW ranks higher than August HW here as the ESI weights humidity less. The most distinct difference between the two HWs is observed during the midday and afternoon hours, where the September HW maintained a higher ΔESI peak than the August HW by nearly 4°C because of higher temperatures. Although WBT is sufficient to characterize the heat stress experienced by most urban inhabitants who can stay indoors or seek shade during heatwave days, as ESI also accounts for the effect of direct solar radiation, it is particularly relevant for people who work outdoors in a low-shade Southern California environment.

b. Intraurban spatial heterogeneity of heatwave impact

For the clustering analysis, we only focus on the diurnal trend of excess air temperature (ΔNSAT) and excess heat stress (ΔWBT). We identified three distinct contiguous regions that have different response patterns to HWs (Fig. 7a). The emergent spatial clusters are 1) Southern LA and Orange County, which are cooler and more influenced by the availability of coastal moisture; 2) San Fernando, San Gabriel, San Bernardino, and Riverside Valley regions, which are drier and hotter; and 3) the central region of LA from Santa Monica to about 30 km east of downtown LA, which falls in between the two extremes.

We first discuss the spatially clustered air temperature trends for HW versus non-HW scenarios (Figs. 8a–d). The spatial heterogeneity in air temperatures across the 3 regions is most prominent during the daytime, with southern LA showing cooler temperatures than the valley regions by up to 5°C (Figs. 8a,b). These relative regional differences were captured overall well by WRF. Note however that temperatures in the coastal regions near Santa Monica were overestimated (section 3b) due to the influence of a mild sea breeze; in observations, the Santa Monica coastal region would be likely be grouped with the Southern LA spatial cluster. WRF indicates that all regions experience temperatures up to 5°C warmer during the August HW and nearly 12°C warmer during the September HW during the daytime, thereby maintaining or slightly enhancing the non-HW spatial thermal gradients This is seen as well in ERA5-Land (Fig. S8 in the online supplemental material). The nighttime air temperatures are more spatially homogeneous. From the model output, we note that the nighttime signature of heatwaves (characterized by ΔNSAT in Figs. 8c,d) was observed most strongly in the urbanized inland valleys. Note that the model output had a positive bias of nearly 4°C in the valley regions due to a systematic underestimation of nighttime temperatures. However, the ΔNSAT variable focusses on the difference between the HW and non-HW days and as a result remains unaffected by the bias. We find that the valley regions still have strong ΔNSAT during nighttime (Figs. S8 and S9 in the online supplemental material).

In terms of heat stress (Figs. 8e–h), the main distinction in the diurnal thermal cycle of WBT across the 3 regions can be seen in the non-HW scenario, especially at night. Despite the higher air temperatures (during the daytime), the valley regions display a similar or lower level of heat stress due to dry conditions, whereas cooler southern LA usually has a higher heat stress despite its lower temperatures due to greater humidity from the coastal winds that advect the "marine layer" onshore (Figs. 8e,f). This influence of more-humid conditions is especially noticeable at night. With less nighttime radiational cooling, the diurnal range of WBT for each region as well as the WBT difference across the 3 clusters reduces due to the August HW in particular. The impact of this ΔWBT is
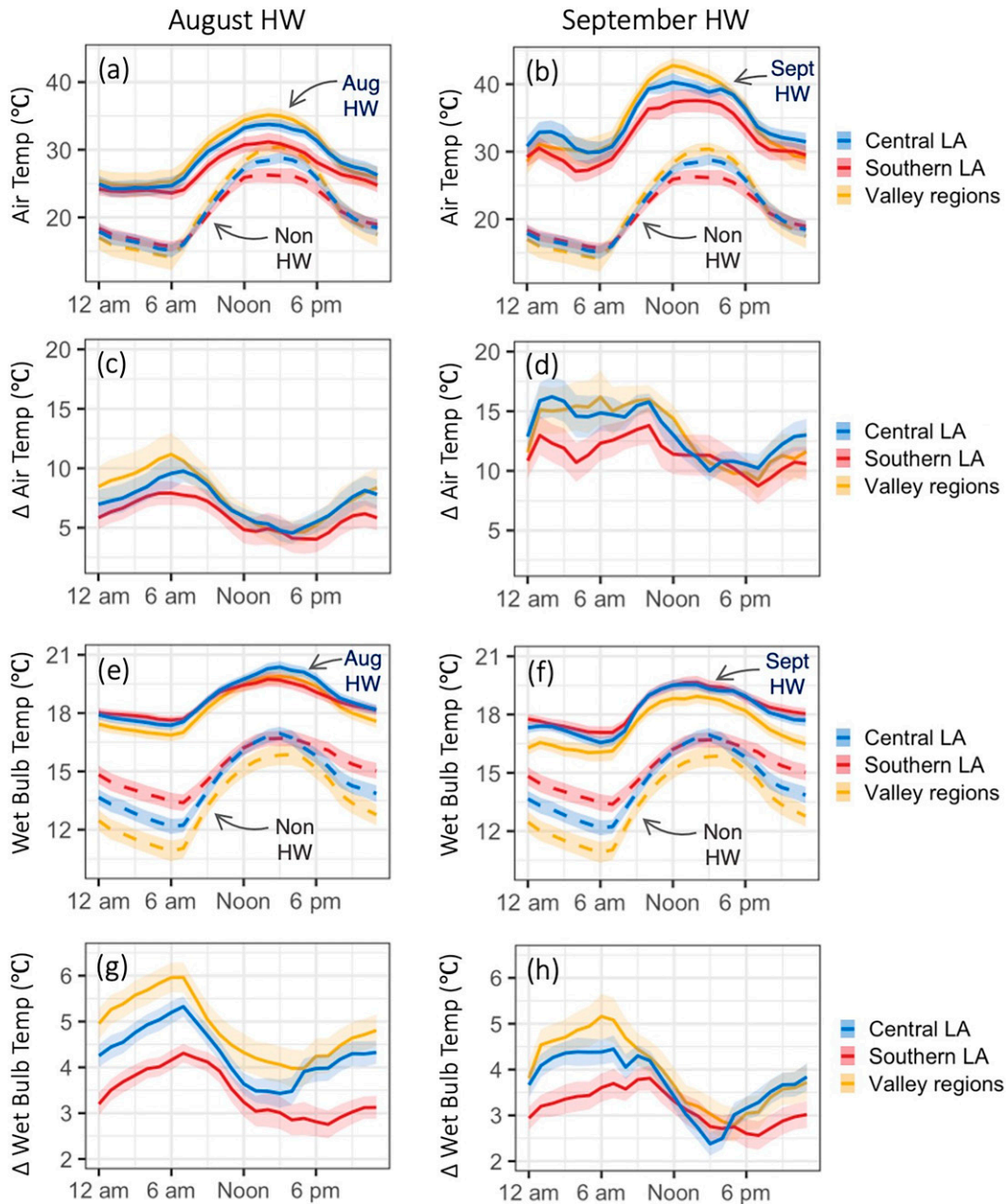
FIG. 8. The diurnal trends of NSAT, WBT, as well as ΔNSAT and ΔWBT (computed in the same way as in Fig. 5) for the three spatial clusters: (left) August HW; (right) September HW. The solid line indicates the mean (computed as spatial mean over urban areas and then hour-specific averaged over the identified HW or non-HW days), and the colored ribbon corresponds to ±1 standard deviation for each of the variables.

most evident in the valley regions, where it is significantly higher than in Southern LA. WRF is able to capture the different aspects of the August HW signature well (Fig. S8 in the online supplemental material). However, it misses the fact that the dry September HW did not meaningfully impede nighttime cooling and therefore saw little deviation from the non-HW diurnal cycle (Figs. S8 and S9 in the online supplemental material). Challenges in representing urban land cover, local downslope warming, and coastal air infiltration

may also be in play—a complex array of factors that affects other regions as well, such as the Pacific Northwest (White et al. 2023).

5. Summary

Our examination of two contrasting heatwaves in Southern California highlights the importance of subtle differences in meteorological forcings for shaping the character of heatwaves, including interactions with UHIs in complex geographical terrain.

As the region's summertime climate is usually characterized by hot and dry conditions (such as those heightened by Santa Ana winds), we demonstrate here that the persistent hot and humid HW such as August 2020 can yield higher humid heat in both coastal and inland areas. This result highlights the potential discrepancy between the popular conception of an extreme-weather threat (in this case, from extreme heat characterized simply by air temperature) and the human-health-centric manifestations of extreme heat (characterized by wet-bulb temperature and environmental stress index).

We find that the impact of HWs is more accurately assessed by focusing on the anomalies of each heat stress metric, characterized as ΔWBT. In the two cases considered, both dry and humid HWs add to the heat stress in each neighborhood by 2°–6°C. But they also serve as a synoptic scale forcing that serves, especially in the case of the August event, to homogenize heat stress *gradient* over urban areas of the LA region spatially and diurnally, relative to non-HW local gradients. The spatial and temporal portraits of the two HWs we have created would be valuable to extend to other observed and projected HWs in this region, to assess the fine-scale patterns of the anticipated more humid nighttime events.

Our results illustrate how several dimensions of HW analysis and several sources of information with complementary strengths are needed to fully understand which subregions suffer the most disproportionate impacts of a regionwide HW and why. HW anomalies, urban microclimate, and particular meteorological forcings, as well as the usage of both temperature and heat stress metrics, are necessary to capture HW effects on acclimated individuals within different urban neighborhoods. Last, model outputs such as WRF have limitations in definitive analyses on urban microclimates and more intensive in situ heat stress observations will be crucial in future studies. Our work may also reflect on other coastal Mediterranean and semiarid climates, and on WRF/reanalysis/observation UHI comparisons more broadly. More work needs to be done to understand precisely how these competing metrics can best identify the vulnerable people or systems at greatest risk of heat-related impacts across the diverse geographies of metropolitan Los Angeles to aid in fine-tuning infrastructure investment and emergency response plans at the neighborhood level.

Data availability statement. The WRF code used to simulate the heatwaves, along with the model outputs (netCDF format), will be made available upon request to the authors.

REFERENCES

Baldwin, J. W., J. B. Dessy, G. A. Vecchi, and M. Oppenheimer, 2019: Temporally compound heat wave events and global warming: An emerging hazard. *Earth's Future*, **7**, 411–427, https://doi.org/10.1029/2018EF000989.

Black, E., M. Blackburn, G. Harrison, B. Hoskins, and J. Methven, 2004: Factors contributing to the summer 2003 European heatwave. *Weather*, **59**, 217–223, https://doi.org/10.1256/wea.74.04.

Borg, M. A., and Coauthors, 2021: Occupational heat stress and economic burden: A review of global evidence. *Environ. Res.*, **195**, 110781, https://doi.org/10.1016/j.envres.2021.110781.

Brown, S. J., 2020: Future changes in heatwave severity, duration and frequency due to climate change for the most populous cities. *Wea. Climate Extremes*, **30**, 100278, https://doi.org/10.1016/j.wace.2020.100278.

Buzan, J. R., and M. Huber, 2020: Moist heat stress on a hotter Earth. *Annu. Rev. Earth Planet. Sci.*, **48**, 623–655, https://doi.org/10.1146/annurev-earth-053018-060100.

——, K. Oleson, and M. Huber, 2015: Implementation and comparison of a suite of heat stress metrics within the Community Land Model version 4.5. *Geosci. Model Dev.*, **8**, 151–170, https://doi.org/10.5194/gmd-8-151-2015.

Cedeño Laurent, J. G., A. Williams, Y. Oulhote, A. Zanobetti, J. G. Allen, and J. D. Spengler, 2018: Reduced cognitive function during a heat wave among residents of non-air-conditioned buildings: An observational study of young adults in the summer of 2016. *PLOS Med.*, **15**, e1002605, https://doi.org/10.1371/journal.pmed.1002605.

Chen, F., and Coauthors, 2011: The integrated WRF/urban modelling system: Development, evaluation, and applications to urban environmental problems. *Int. J. Climatol.*, **31**, 273–288, https://doi.org/10.1002/joc.2158.

Dunne, J. P., R. J. Stouffer, and J. G. John, 2013: Reductions in labour capacity from heat stress under climate warming. *Nat. Climate Change*, **3**, 563–566, https://doi.org/10.1038/nclimate1827.

Gershunov, A., and K. Guirguis, 2012: California heat waves in the present and future. *Geophys. Res. Lett.*, **39**, L18710, https://doi.org/10.1029/2012GL052979.

——, D. R. Cayan, and S. F. Iacobellis, 2009: The great 2006 heat wave over California and Nevada: Signal of an increasing trend. *J. Climate*, **22**, 6181–6203, https://doi.org/10.1175/2009JCLI2465.1.

——, and Coauthors, 2021: Hot and cold flavors of Southern California's Santa Ana winds: Their causes, trends, and links with wildfire. *Climate Dyn.*, **57**, 2233–2248, https://doi.org/10.1007/s00382-021-05802-z.

Goodman, J., M. Hurwitz, J. Park, and J. Smith, 2019: Heat and learning. NBER Working Paper 24639, 60 pp., https://www.nber.org/system/files/working_papers/w24639/w24639.pdf.

Gutierrez, A. A., S. Hantson, B. Langenbrunner, B. Chen, Y. Jin, M. L. Goulden, and J. T. Randerson, 2021: Wildfire response to changing daily temperature extremes in California's Sierra Nevada. *Sci. Adv.*, **7**, eabe6417, https://doi.org/10.1126/sciadv.abe6417.

Hulley, G. C., B. Dousset, and B. H. Kahn, 2020: Rising trends in heatwave metrics across Southern California. *Earth's Future*, **8**, e2020EF001480, https://doi.org/10.1029/2020EF001480.

Laaidi, K., A. Zeghnoun, B. Dousset, P. Bretin, S. Vandentorren, E. Giraudet, and P. Beaudeau, 2012: The impact of heat islands on mortality in Paris during the August 2003 heat wave. *Environ. Health Perspect.*, **120**, 254–259, https://doi.org/10.1289/ehp.1103532.

Lee, Y.-Y., and R. Grotjahn, 2016: California Central Valley heat waves form two ways. *J. Climate*, **29**, 1201–1217, https://doi.org/10.1175/JCLI-D-15-0270.1.

Lesk, C., E. Coffel, J. Winter, D. Ray, J. Zscheischler, S. I. Seneviratne, and R. Horton, 2021: Stronger temperature-moisture couplings exacerbate the impact of climate warming

on global crop yields. *Nat. Food*, **2**, 683–691, https://doi.org/10.1038/s43016-021-00341-6.

Meehl, G. A., and C. Tebaldi, 2004: More intense, more frequent, and longer lasting heat waves in the 21st century. *Science*, **305**, 994–997, https://doi.org/10.1126/science.1098704.

Mora, C., and Coauthors, 2017: Global risk of deadly heat. *Nat. Climate Change*, **7**, 501–506, https://doi.org/10.1038/nclimate3322.

Moran, D. S., K. B. Pandolf, Y. Shapiro, Y. Heled, Y. Shani, W. T. Mathew, and R. R. Gonzalez, 2001: An environmental stress index (ESI) as a substitute for the wet bulb globe temperature (WBGT). *J. Therm. Biol.*, **26**, 427–431, https://doi.org/10.1016/S0306-4565(01)00055-9.

Orth, R., O. Sungmin, J. Zscheischler, M. D. Mahecha, and M. Reichstein, 2022: Contrasting biophysical and societal impacts of hydro-meteorological extremes. *Environ. Res. Lett.*, **17**, 014044, https://doi.org/10.1088/1748-9326/ac4139.

Parsons, L. A., Y. J. Masuda, T. Kroeger, D. Shindell, N. H. Wolff, and J. T. Spector, 2022: Global labor loss due to humid heat exposure underestimated for outdoor workers. *Environ. Res. Lett.*, **17**, 014050, https://doi.org/10.1088/1748-9326/ac3dae.

Perkins-Kirkpatrick, S. E., and S. C. Lewis, 2020: Increasing trends in regional heatwaves. *Nat. Commun.*, **11**, 3357–, https://doi.org/10.1038/s41467-020-16970-7.

Pierce, D. W., T. P. Barnett, K. M. AchutaRao, P. J. Gleckler, J. M. Gregory, and W. M. Washington, 2006: Anthropogenic warming of the oceans: Observations and model results. *J. Climate*, **19**, 1873–1900, https://doi.org/10.1175/JCLI3723.1.

Raymond, C., D. Singh, and R. M. Horton, 2017: Spatiotemporal patterns and synoptics of extreme wet-bulb temperature in the contiguous United States. *J. Geophys. Res. Atmos.*, **122**, 13 108–13 124, https://doi.org/10.1002/2017JD027140.

——, and Coauthors, 2019: Projections and hazards of future extreme heat. *The Oxford Handbook of Planning for Climate Change Hazards*. W. T. Pfeffer, J. B. Smith, and K. L. Ebi, Eds., Oxford University Press, 6–11.

——, T. Matthews, and R. M. Horton, 2020: The emergence of heat and humidity too severe for human tolerance. *Sci. Adv.*, **6**, eaaw1838, https://doi.org/10.1126/sciadv.aaw1838.

Robinson, P. J., 2001: On the definition of a heat wave. *J. Appl. Meteor.*, **40**, 762–775, https://doi.org/10.1175/1520-0450(2001)040<0762:OTDOAH>2.0.CO;2.

Safford, H. D., A. K. Paulson, Z. L. Steel, D. J. N. Young, and R. B. Wayman, 2022: The 2020 California fire season: A year like no other, a return to the past or a harbinger of the future? *Global Ecol. Biogeogr.*, **31**, 2005–2025, https://doi.org/10.1111/geb.13498.

Schwingshackl, C., J. Sillmann, A. M. Vicedo-Cabrera, M. Sandstad, and K. Aunan, 2021: Heat stress indicators in CMIP6: Estimating future trends and exceedances of impact-relevant thresholds. *Earth's Future*, **9**, e2020EF001885, https://doi.org/10.1029/2020EF001885.

Sherwood, S. C., and M. Huber, 2010: An adaptability limit to climate change due to heat stress. *Proc. Natl. Acad. Sci. USA*, **107**, 9552–9555, https://doi.org/10.1073/pnas.0913352107.

Shreevastava, A., P. S. C. Rao, and G. S. McGrath, 2019a: Emergent self-similarity and scaling properties of fractal intra-urban heat islets for diverse global cities. *Phys. Rev.*, **100E**, 032142, https://doi.org/10.1103/PhysRevE.100.032142.

——, S. Bhalachandran, G. S. McGrath, M. Huber, and P. S. C. Rao, 2019b: Paradoxical impact of sprawling intra-urban heat islets: Reducing mean surface temperatures while enhancing local extremes. *Sci. Rep.*, **9**, 19681, https://doi.org/10.1038/s41598-019-56091-w.

——, S. Prasanth, P. Ramamurthy, and P. S. C. Rao, 2021: Scale-dependent response of the urban heat island to the European heatwave of 2018. *Environ. Res. Lett.*, **16**, 104021, https://doi.org/10.1088/1748-9326/ac25bb.

Sobstyl, J. M., T. Emig, M. J. Abdolhosseini Qomi, F.-J. Ulm, and R. J.-M. Pellenq, 2018: Role of city texture in urban heat islands at nighttime. *Phys. Rev. Lett.*, **120**, 108701, https://doi.org/10.1103/PhysRevLett.120.108701.

Speizer, S., C. Raymond, C. Ivanovich, and R. M. Horton, 2022: Concentrated and intensifying humid heat extremes in the IPCC AR6 regions. *Geophys. Res. Lett.*, **49**, e2021GL097261, https://doi.org/10.1029/2021GL097261.

Stipanuk, G. S., 1973: Algorithms for generating a skew-T, log p diagram and computing selected meteorological quantities. Tech. Rep. AD-769 739, 41 pp., https://apps.dtic.mil/sti/pdfs/AD0769739.pdf.

Stone, B., Jr., and Coauthors, 2021: Compound climate and infrastructure events: How electrical grid failure alters heat wave risk. *Environ. Sci. Technol.*, **55**, 6957–6964, https://doi.org/10.1021/acs.est.1c00024.

Tamrazian, A., S. LaDochy, J. Willis, and W. C. Patzert, 2008: Heat waves in Southern California: Are they becoming more frequent and longer lasting? *Yearb. Assoc. Pac. Coast Geogr.*, **70**, 59–69, https://doi.org/10.1353/pcg.0.0001.

Vahmani, P., and G. Ban-Weiss, 2016: Impact of remotely sensed albedo and vegetation fraction on simulation of urban climate in WRF-urban canopy model: A case study of the urban heat island in Los Angeles. *J. Geophys. Res. Atmos.*, **121**, 1511–1531, https://doi.org/10.1002/2015JD023718.

Vanos, J. K., and A. J. Grundstein, 2020: Variations in athlete heat-loss potential between hot-dry and warm-humid environments at equivalent wet-bulb globe temperature thresholds. *J. Athl. Train.*, **55**, 1190–1198, https://doi.org/10.4085/1062-6050-313-19.

Vant-Hull, B., and Coauthors, 2018: The Harlem Heat Project: A unique media-community collaboration to study indoor heat waves. *Bull. Amer. Meteor. Soc.*, **99**, 2491–2506, https://doi.org/10.1175/BAMS-D-16-0280.1.

Vecellio, D., S. T. Wolf, R. M. Cottle, and W. L. Kenney, 2022: Evaluating the 35°C wet-bulb temperature adaptability threshold for young, healthy subject (PSU HEAT Project). *J. Appl. Physiol.*, **132**, 340–345, https://doi.org/10.1152/japplphysiol.00738.2021.

Vicedo-Cabrera, A. M., and Coauthors, 2021: The burden of heat-related mortality attributable to recent human-induced climate change. *Nat. Climate Change*, **11**, 492–500, https://doi.org/10.1038/s41558-021-01058-x.

White, R. H., and Coauthors, 2023: The unprecedented Pacific Northwest heatwave of June 2021. *Nat. Commun.*, **14**, 727, https://doi.org/10.1038/s41467-023-36289-3.

Zhao, L., M. Oppenheimer, Q. Zhu, J. W. Baldwin, K. L. Ebi, E. Bou-Zeid, K. Guan, and X. Liu, 2018: Interactions between urban heat islands and heat waves. *Environ. Res. Lett.*, **13**, 034003, https://doi.org/10.1088/1748-9326/aa9f73.

Zhou, B., D. Rybski, and J. P. Kropp, 2017: The role of city size and urban form in the surface urban heat island. *Sci. Rep.*, **7**, 4791, https://doi.org/10.1038/s41598-017-04242-2.